

A semi-automated method for identifying and measuring myelinated nerve fibers in scanning electron microscope images

Heather L. More^{a,*}, Jingyun Chen^{b,1}, Eli Gibson^b, J. Maxwell Donelan^a, Mirza Faisal Beg^b

^a Department of Biomedical Physiology & Kinesiology, Simon Fraser University, 8888 University Drive, Burnaby, BC V5A 1S6, Canada

^b School of Engineering Science, Simon Fraser University, 8888 University Drive, Burnaby, BC V5A 1S6, Canada

ARTICLE INFO

Article history:

Received 7 October 2010

Received in revised form 15 July 2011

Accepted 27 July 2011

Keywords:

Image segmentation

Axon

Myelin

Nerve

Semi-automated

Scanning electron microscope

ABSTRACT

Diagnosing illnesses, developing and comparing treatment methods, and conducting research on the organization of the peripheral nervous system often require the analysis of peripheral nerve images to quantify the number, myelination, and size of axons in a nerve. Current methods that require manually labeling each axon can be extremely time-consuming as a single nerve can contain thousands of axons. To improve efficiency, we developed a computer-assisted axon identification and analysis method that is capable of analyzing and measuring sub-images covering the nerve cross-section, acquired using a scanning electron microscope. This algorithm performs three main procedures – it first uses cross-correlation to combine the acquired sub-images into a large image showing the entire nerve cross-section, then identifies and individually labels axons using a series of image intensity and shape criteria, and finally identifies and labels the myelin sheath of each axon using a region growing algorithm with the geometric centers of axons as seeds. To ensure accurate analysis of the image, we incorporated manual supervision to remove mislabeled axons and add missed axons. The typical user-assisted processing time for a two-megapixel image containing over 2000 axons was less than 1 h. This speed was almost eight times faster than the time required to manually process the same image. Our method has proven to be well suited for identifying axons and their characteristics, and represents a significant time savings over traditional manual methods.

© 2011 Elsevier B.V. All rights reserved.

1. Introduction

Peripheral nerves, such as the sciatic nerve in the leg, are responsible for the essential task of conducting information about sensation and movement between the central nervous system and the rest of the body. Consequently, there are hundreds of studies investigating the structure and function of these nerves, their reaction to injury, and mechanisms of regrowth. Many of these studies rely on measurements of nerve characteristics such as the number and size of nerve cell projections known as axons (e.g. Gasser and Grundfest, 1939; Hursh, 1939; Edds, 1950; Fried and Hildebrand, 1982; Knox et al., 1989; Wattig et al., 1992; Sullivan et al., 2003; Demirel et al., 2006). In vertebrates, an insulating sheath known as myelin typically surrounds large axons. Myelin thickness is related to the speed at which an axon can transmit electrical impulses (Rushton, 1951; Arbuthnott et al., 1980b), and for this reason myelin sheath characteristics are also of interest (Webster, 1971; Arbuthnott et al., 1980a,b; Fried and Hildebrand,

1982; Fried et al., 1982; Smith et al., 1982; Friede and Beuche, 1985; Demirel et al., 2006). Axon and myelin characteristics are commonly found using images of nerve cross-sections in which the tissue has been stained to visualize cell membranes and myelin. These visible structures are then identified and measured. This process of identifying and labeling regions of interest in an image is known as segmentation. Given that a single nerve can contain many thousands of axons and that an application can require the analysis of tens or hundreds of nerves (Schmalbruch, 1986; Vogt, 1996), it is important to develop methods to obtain the needed measurements efficiently from nerve images.

There are many methods for segmenting images of nerve cross-sections. Before the advent of computers, photographs of several representative sample areas from each nerve cross-section were printed out on large sheets of film or paper, and the axons identified and measured by hand (Webster, 1971; Hildebrand and Hahn, 1978; Boyd and Kalu, 1979; Arbuthnott et al., 1980a,b; Fraher, 1980; Fried and Hildebrand, 1982; Fried et al., 1982). By extrapolating from these sample areas to the whole nerve, the axonal characteristics of the nerve were approximated. Due to the time-consuming nature of this completely manual method, it was generally not feasible to analyze the entire nerve cross-section but only small sections.

* Corresponding author. Tel.: +1 778 782 4986; fax: +1 778 782 3040.
E-mail address: hmore@sfu.ca (H.L. More).

¹ These authors contributed equally to this work.

With the advent of more advanced computer technology, it was possible to manually identify and trace each axon in several representative sample areas using a computerized stylus or tablet on a printout or computer screen, and then program the computer to calculate the relevant measurements (Dunn et al., 1975; Bronson and Hedley-Whyte, 1977; Karnes et al., 1977; Smith et al., 1982; Friede and Beuche, 1985; Friede, 1986; Schmalbruch, 1986; Ewart et al., 1989; Hoffmeister et al., 1991). As hardware and software improvements continue to be made and new types of algorithms are developed, it has become possible to automatically identify, rather than manually trace, most or all of the axons in digital images. Algorithms using techniques such as template matching (Frykman et al., 1979), edge detection (Ellis et al., 1980; Zimmerman et al., 1980; Usson et al., 1991), active contours (Fok et al., 1996), zonal graphs (Romero et al., 2000), neural networks (Jurrus et al., 2010), and region growing (Zhao et al., 2010) have been produced to automatically identify axons and myelin in nerve images based on their shape or grey-level characteristics. These methods are faster than manual techniques, allowing more sample areas to be analyzed – for example, the measurement of 1000 axons can be reduced from 1 day to 1 h (Usson et al., 1991). In some cases, especially in the case of smaller nerves, these more efficient methods allow analysis of all axons in the nerve cross-section (Usson et al., 1991; Romero et al., 2000; Weyn et al., 2005). There have even been several studies using advanced segmentation techniques to identify and track axons in three-dimensional image sets (Jeong et al., 2009; Jurrus et al., 2010). Still, many approaches require specialized equipment, such proprietary analysis systems (e.g. Hunter et al., 2007). Few methods are entirely automated as some form of user input, for example manual addition or deletion of axons, is generally required to ensure accuracy. In fact, because of the inherent variability present in biological samples, manual confirmation of the results through the process of supervised segmentation is often desirable (Zimmerman et al., 1980; Auer, 1994).

Analyzing several sample areas from a nerve, rather than whole-nerve images, to obtain values representative of the whole nerve can introduce bias into the results. Because of their size, larger axons are more likely to intersect the edge of the sample area and be cut off, making the results biased towards small fibers (Larsen, 1998). As well, the size distribution of axons can vary in different parts of the nerve, with some areas having a higher percentage of large axons and other areas having a higher percentage of small axons (Saxod et al., 1985; Torch et al., 1989a). While these problems can be ameliorated by using more and larger sample areas, and appropriate sampling strategies, accuracy and effectiveness could be greatly improved by analyzing all axons within a nerve rather than extrapolating whole-nerve values from a limited number of sample areas (Saxod et al., 1985; Torch et al., 1989a).

Most work on segmentation of nerve images has focused on light microscope images (Dunn et al., 1975; Frykman et al., 1979; Ellis et al., 1980; Zimmerman et al., 1980; Usson et al., 1991; Auer, 1994; Mezin et al., 1994; Campadelli et al., 1999; Romero et al., 2000; Weyn et al., 2005; Urso-Baiarda and Grobbelaar, 2006; Hunter et al., 2007) or, less commonly, transmission electron microscope (TEM) images (Vogt, 1996; Vogt and Trenkle, 1998; Jurrus et al., 2010; Zhao et al., 2010). Light microscopy uses easily available low-cost equipment, while TEM is higher-cost and requires more specialized equipment but is capable of very high-resolution images (Bronson et al., 1978). Both these methods require samples to be cut into thin slices, which can be very difficult in large-diameter nerves. In addition, TEM imaging is only possible for samples of less than 3 mm in diameter, which would require large-diameter nerves to be divided into several smaller samples. A good alternative to light microscopy and TEM is the use of a scanning electron microscope (SEM). Unlike TEM imaging, which produces images by detecting electrons passed through the sample, SEM imaging produces images by detecting

electrons bounced off the surface of the sample. This technique allows thicker sections to be imaged than either of the previous two methods and can therefore be used to effectively image larger-diameter nerves in which thin sections would be difficult to prepare without specialized equipment. It is also capable of imaging sample areas of several centimeters in diameter, eliminating the need to divide large-diameter nerve samples. While there have been a number of segmentation and analysis methods developed for light microscope and TEM images, to our knowledge, there has been no robust method developed to analyze whole-nerve images acquired using an SEM.

Our goal was to develop an efficient method for quantifying axon and myelin size distributions in an image of an entire nerve cross-section. We chose SEM imaging to enable examination of an entire nerve cross-section including those of nerves that are very large. For ease of use, we required that our algorithm be simple, intuitive, and not necessitate the use of proprietary software. To ensure accuracy and enable operator verification, we chose a supervised semi-automated method to segment axons and myelin in the SEM images, then used the resulting data to determine nerve fiber number, size, and myelination. In the remainder of this paper, we first present details of our method's six main steps: image acquisition, image stitching, axon segmentation, myelin segmentation, quality control, and data output. We then demonstrate the method's performance in analyzing a single rat fascicle and discuss its strengths and limitations.

2. Methods

2.1. Image acquisition

Following standard methods of sample preparation, we acquired sciatic nerve samples from a rat perfused with fixative containing 4% paraformaldehyde and 1% glutaraldehyde then further preserved the samples in the same fixative before staining them with osmium tetroxide and embedding them in plastic resin (More et al., 2010). A Bausch & Lomb 2100 Nanolab SEM imaged the embedded nerves at 1665 \times magnification to obtain 512 \times 477 pixel images. The microscope scanned at 10 kV using a spot size of 7, the 'low 6' resolution setting, and the backscatter detector. Prior to nerve imaging, we confirmed the accuracy of the microscope scalebar with a standard test sample of known size. Nerves had total diameters of approximately 1.75 mm, with fascicle diameters ranging from approximately 0.1 mm to approximately 1 mm. Due to instrument limitations, we could not acquire one single image of the entire nerve cross-section but instead scanned through the cross-section to obtain a set of overlapping sub-images with identical size and resolution. The amount of overlap on each side of each sub-image was approximately 12–20% of the sub-image size to allow sufficient overlap to align adjacent images and allow cropping.

2.2. Image stitching

SEM imaging produced a set of sub-images for each nerve cross-section which fit together in an overlapping grid-like fashion, with the approximate position of each sub-image known. The edges of the sub-images were cropped before further processing to remove presence of edge distortion. To combine the cropped sub-images into one image showing the entire nerve cross-section, we developed an algorithm which used normalized cross-correlation to align the sub-images and stitch them together into a single image (Fig. 1). While other studies have reported more sophisticated image stitching methods (Tasdizen et al., 2010; Vogt and Trenkle, 1998), we found that cross-correlation was simple, fast,

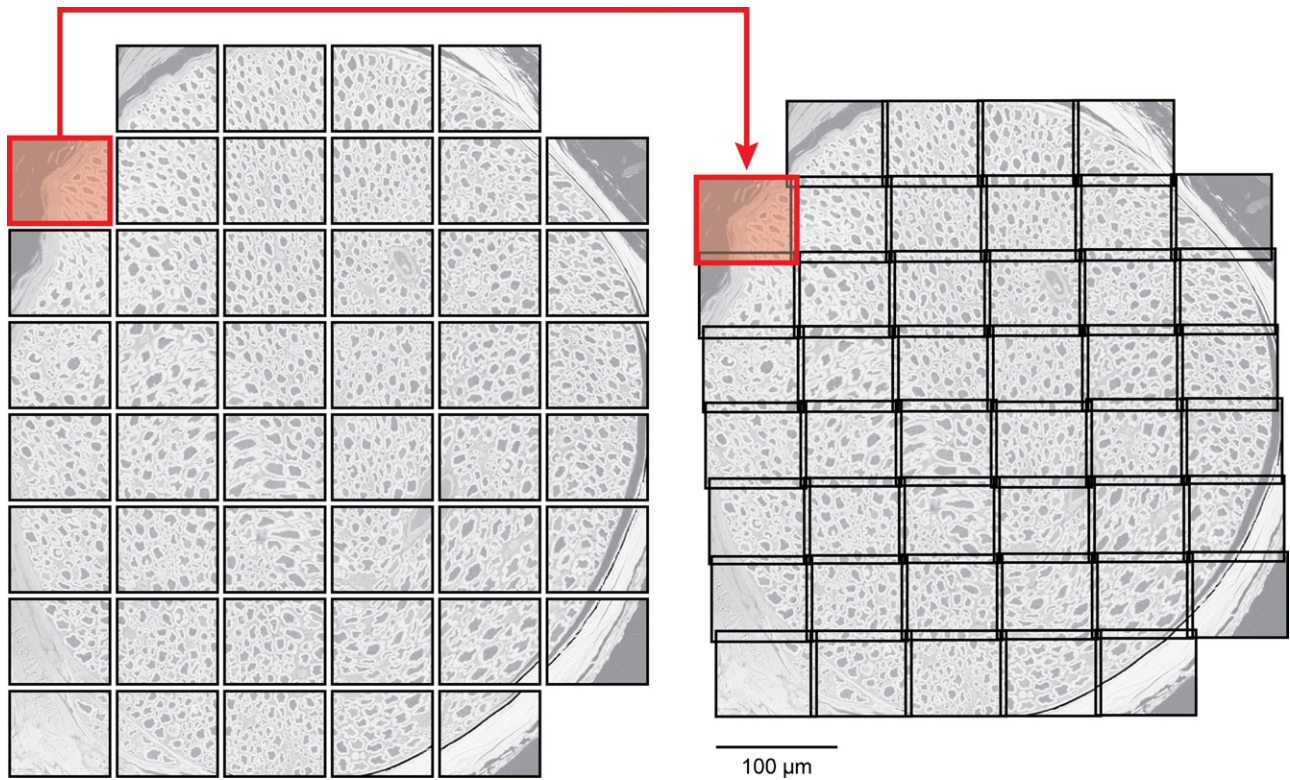


Fig. 1. Stitching of sub-images for one rat fascicle. Overlapping scanning electron microscope (SEM) images are taken sequentially to cover the entire fascicle (left), then stitched together using cross-correlation into one image of the entire fascicle (right). All images are shown at the same scale.

and accurate for our images. To accomplish this, each sub-image was compared to an overlapping section of the neighboring sub-image. This overlapping section was termed the template. The template was translated over the entire area of its neighboring sub-image, termed the target, with the position of the target remaining fixed. A normalized cross-correlation index describing the similarity of pixel values between the overlapping regions of the template and the target was calculated at each translation (Haralick and Shapiro, 1992; Lewis, 1995). We considered only translations, as the position of the sample was held fixed throughout the imaging process. The optimal position of the template with respect to the target was the position at which the normalized cross-correlation index was maximal. This optimal position was used to stitch the sub-images together so that there was the highest similarity possible between the overlapping regions. Mathematically, if I_0 and I_1 are the template and target, respectively, the normalized cross-correlation of these images as a function of their relative horizontal position u and vertical position v is given by:

Normalized cross-correlation(u, v)

$$= \frac{\sum_{x,y} (I_0(x-u, y-v) - \bar{I}_0(u, v))(I_1(x, y) - \bar{I}_1(u, v))}{\sum_{x,y} (I_0(x-u, y-v) - \bar{I}_0(u, v))^2 \sum_{x,y} (I_1(x, y) - \bar{I}_1(u, v))^2}$$

where $\bar{I}_0(u, v)$ and $\bar{I}_1(u, v)$ are the mean pixel values of the template and target, respectively, over the overlap region and are expressed as a function of displacement position. The algorithm first aligned all sub-images in each row, then aligned the rows with each other to create the final image.

2.3. Axon segmentation

Stitched images showing entire nerve fascicles were identified and labeled using a combination of automatic and manual

techniques, referred to as supervised segmentation. We manually cropped each stitched fascicle image to remove extraneous surrounding information and analyzed each fascicle individually to enable slight adjustments of parameter values such as thresholds. The steps of our algorithm are illustrated in Fig. 2.

Images of nerve cross-sections acquired using an SEM show axons as dark areas surrounded by a lighter ring of myelin, all on a grey background. These intensity characteristics can be used to automatically identify axons and myelin using a series of morphological operations to transform images. Morphological operations transform images by iteratively carrying out set operations (such as the union, intersection, or complement) between the image and a smaller geometric shape (such as a circle or square) known as a structuring element. The four basic morphological operations are *dilation* which expands light areas, *erosion* which shrinks light areas, *opening* which removes small light areas by performing erosion followed by dilation, and *closing* which removes small dark areas by performing dilation followed by erosion. Combinations of morphological operations are commonly used to identify particles in various types of applications, but comparatively few studies have focused on using these concepts to analyze nerve images (Torch et al., 1989b; Vogt, 1996; McCreery et al., 1997; Vogt and Trenkle, 1998; Romero et al., 2000; Hunter et al., 2007).

Morphological reconstructions transform images using a sequence of morphological and set operations. One image, denoted the marker, is dilated or eroded before being compared to the second image, denoted the mask. Areas present in both images are retained in the marker, whereas areas present only in one of the images are not. This process is repeated, with each successive dilation or erosion being compared to the mask, until there is no further change in the marker image. The typical structuring element for these procedures is a nine-element square which defines connectivity – the central element denotes a representative pixel of the image and the eight surrounding elements denote the eight

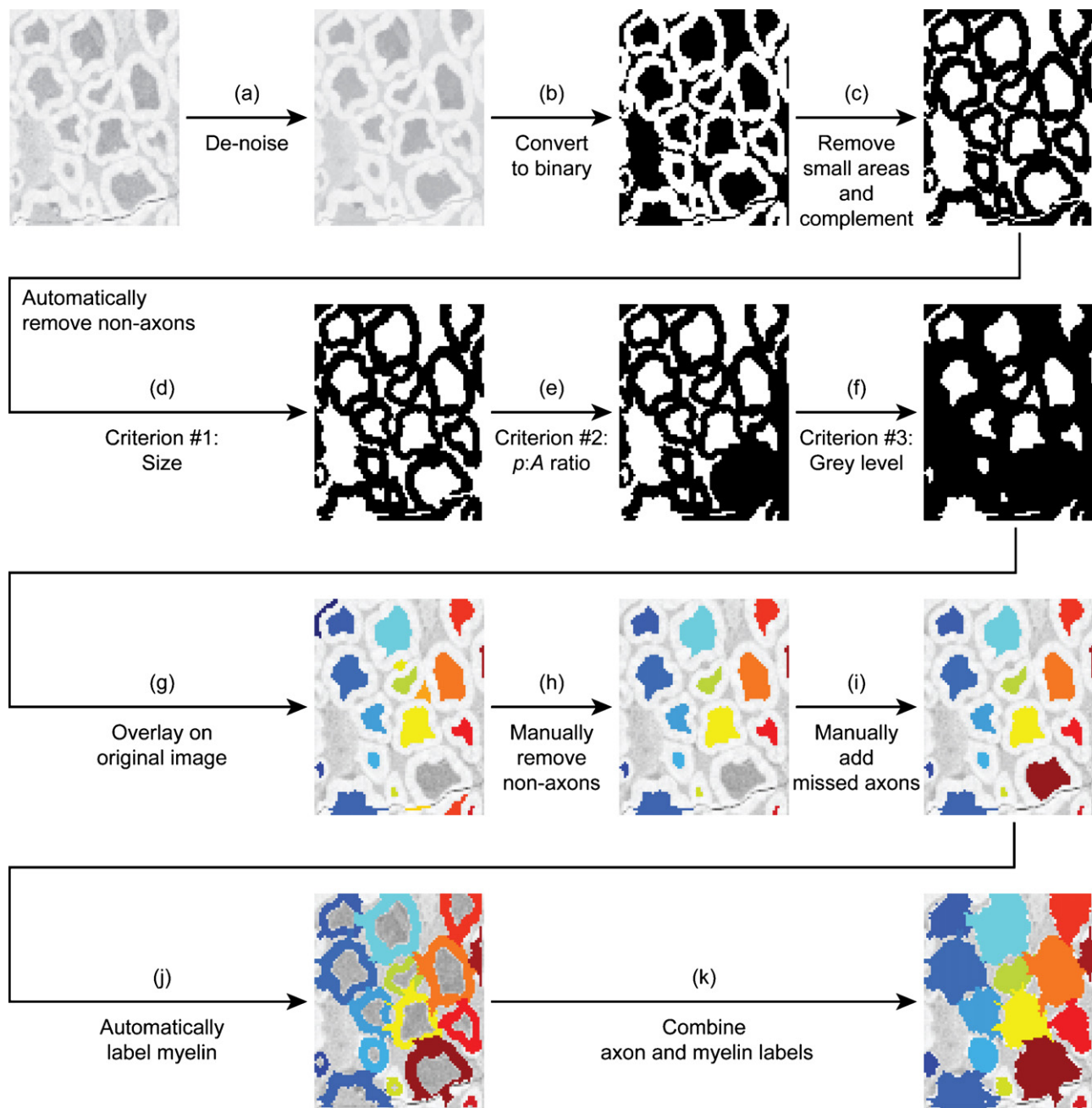


Fig. 2. Axon and myelin segmentation. The original greyscale image is first de-noised (a), then thresholded to convert it to black and white (b). Any remaining small white areas are removed, and the complement is taken (c). Three criteria are used to determine which white connected components are potential axons: first, they must be within a certain size range (d); second, they must have a perimeter to area ratio below a given threshold (e); and third, they must have a low average grey level (f). White connected components meeting these criteria are labeled as potential axons, coloured to enable visualization, and overlaid on the original image for verification by the user (g). Through a graphical user interface, the user is then able to manually remove areas which are not axons (h) and manually add axons which have been missed (i). Using these final axon labels, the algorithm scans radially outwards from the center of each axon to find the surrounding myelin (j). Finally, the labeled area of each axon is combined with its respective myelin area to give labeled nerve fibers (k).

surrounding pixels. These eight elements can each have a value of either 1, meaning the respective pixel is considered connected to the center pixel, or 0, meaning the respective pixel is not considered connected to the center pixel. The two basic types of morphological reconstruction are *morphological reconstruction by dilation* in which the marker is dilated at each iteration, and *morphological reconstruction by erosion* in which the marker is eroded at each iteration.

Due to the system noise of the SEM, we observed scattered grey-level variations throughout the images. This noise was likely caused by a combination of factors including biological and chemi-

cal variability in the tissue, slight changes in electron emission and detection produced by electrical interference and thermal activity, and small differences in detector sensitivity. The noise decreased the clarity of the boundary between each axon and its surrounding myelin and reduced the uniformity of pixel values within these areas, effects detrimental for accurate segmentation.

To improve accuracy, we used a series of combined morphological operations and morphological reconstructions to de-noise the stitched image before segmentation (Fig. 2(a)) (Vincent, 1993). Our algorithm performed one morphological reconstruction by dilation using an eroded version of the original image as the marker and

the original image as the mask. It then dilated the resulting image and performed a second morphological reconstruction by dilation, using the complement of the dilated image as the marker and the complement of the first reconstruction as the mask. The complement of the result was the de-noised image. The overall result of this de-noising process was to remove small localized areas of higher or lower intensity (noise) and instead bring the intensities of these areas closer to that of the surrounding image. Image de-noising based on morphological reconstruction has the advantage of reducing noise while preserving edges in the image. This is unlike mask-based filtering methods, such as the commonly used Gaussian filter, which rely on convolution and can potentially smooth object edges making subsequent segmentation more difficult.

After reconstruction, our algorithm identified and labeled potential axons in the de-noised image. SEM cross-section images show axons as areas of dark grey (low intensity value) pixels and the surrounding myelin as lighter (high intensity value) pixels. The background area between the myelinated axons has a grey-level value between that of the axons and myelin. Our method set all grey-level values below a user-defined threshold to black and all grey-level values above this threshold to white, thus converting the greyscale image into a black and white image – known as a binary image – showing potential axons as black areas on a white background (Fig. 2(b)). The algorithm removed all white areas too small to represent myelin. It then inverted the image by taking its complement, so that the potential axons were shown as white areas (known as connected components) on a black background (Fig. 2(c)). With this method, our algorithm could identify the majority of axons. However, because the grey-level values of the axons and background can be similar, some background areas were mislabeled as potential axons. To reduce the mislabeling of connected components, we used prior knowledge of axon properties to add the following inclusion/exclusion rules:

a. Number of pixels in a connected component

Myelinated axons have a finite range of possible sizes – a connected component with size outside this user-defined range is not an axon, and therefore designated as part of the background (Fig. 2(d)).

b. Shape of a connected component

Axons generally have approximately round shapes, while background areas can have much more convoluted shapes. We measured the degree of roundness using the parameter $R = p/A$, where p is the number of pixels on the perimeter of a connected component and A is the total area in pixels of that component. With a user-defined upper limit of R for axons above a given size, components with shapes closer to round have smaller R values and are designated as axons, whereas components with more convoluted shapes have larger R values and are designated as part of the background (Fig. 2(e)). Examples of axons with different sizes and relative R values are shown in Fig. 3.

c. Average grey-level value of a connected component

Axons are generally shown as areas of dark grey (low intensity value) pixels in the SEM image, whereas background sections are generally shown as areas of lighter grey (higher intensity value) pixels. To refine the initial axon identification, which relied only on the grey-level values of individual pixels, we found the average grey-level value of each connected component and designated all components with an average value greater than a user-defined

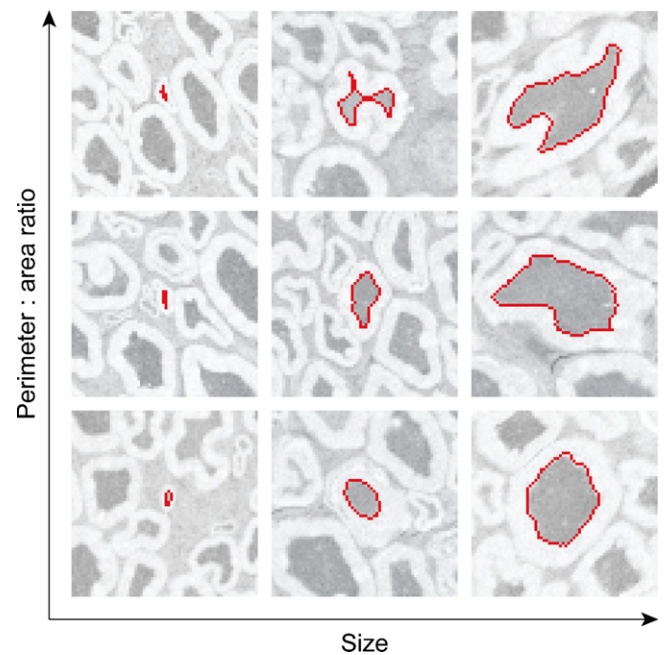


Fig. 3. Examples of the various shapes and sizes of axons detected automatically with our algorithm. We used axon perimeter-to-area ratio as a metric of shape, with axons having more convoluted shapes also having a higher ratio of edge pixels to total pixels. Here, axon perimeter-to-area ratio increases from bottom to top, whereas axon size increases from left to right. Pixels on the perimeter of the identified axon are coloured red.

threshold as part of the background and all components with average grey-levels below this threshold as axons (Fig. 2(f)).

2.4. Myelin segmentation

Once the axons were identified, we used this information to identify the surrounding myelin (Fig. 2(j)). Starting from the geometric center of each identified axon, our method scanned for changes in image intensity along lines radiating outward. Myelin labeling along each scan line began when the radial outward scan line exited the labeled axon area, and terminated when a change in pixel grey-level from high to low, indicating the outer boundary of myelin, was detected. The length of the scanning line, defined by the user, was constrained to be within physiological limits to prevent labeling the myelin of other axons in the case of two myelin areas touching. Upon completion of one scan line, the angle of the scan was incremented and the scan repeated until all 360° of myelin surrounding one axon were scanned. Once this procedure was performed on all axons, morphological closing with a small structuring element was used to smooth and fill in any small gaps in the labeled myelin. A conceptually similar procedure has been previously proposed in the context of cardiac wall segmentation in ultrasound images, denoted as the star algorithm (Yao et al., 2004).

2.5. Quality control

To increase the usability of our method and visualize the computed results, we integrated our algorithms into a user interface which included the ability to input parameters, display the image, and manually correct segmentation results by adding or deleting labeled axons. Input parameters, along with their typical values, are shown in Table 1. Once the segmentation algorithm was complete, automatically segmented axon and myelin areas were colour-labeled for visibility and overlaid on the original image (Fig. 2(g) and (j)). This visualization step was critical to allow the user to evaluate the effectiveness of the chosen parameters and manually

Table 1

Algorithm input parameters for semi-automated segmentation, and their typical values. *Axon binary threshold* defines a threshold for greyscale to binary conversion, and is expressed as a percentage of the greyscale intensity range. *Myelin area* defines the minimum area of regions above threshold for potential myelin areas to be considered myelin rather than noise. *Minimum and maximum axon diameters* define the allowable size range of axon areas, expressed as the diameter of a circle with equivalent area to that of the axon. *Axon major axis* defines the maximum diameter across any part of the axon. *Axon perimeter:area (p:A) ratio* defines the maximum allowable ratio value for axons having areas greater than the minimum size (*Size to enforce p:A ratio*) in which to enforce this criterion. *Fraction of greyscale range to keep* defines the fraction of potential axons to keep after sorting them by their average grey level. *Angle to rotate* defines the angle between adjacent radial search lines when implementing myelin identification using the star algorithm. *Gradient at fiber boundary* defines the minimum change in grey level between two adjacent pixels required to signal the edge of a myelin sheath. *Total fiber diameter* defines the maximum diameter across any part of the nerve fiber. *Myelin thickness* defines the maximum myelin thickness as a proportion of axon diameter. *Structuring element radius* defines the radius of the structuring element used in morphological closing to smooth the labeled myelin sheath.

| Parameter | Typical value | Units |
|--------------------------------------|---------------|-----------------|
| Axon binary threshold | 0.88 | |
| Myelin area (minimum) | 1.2 | μm^2 |
| Axon diameter (minimum) | 1.0 | μm |
| Axon diameter (maximum) | 25 | μm |
| Axon major axis (maximum) | 25 | μm |
| Axon perimeter:area ratio (maximum) | 0.4 | |
| Size to enforce p:A ratio (minimum) | 6.0 | μm |
| Fraction of greyscale range to keep | 0.75 | |
| Angle to rotate | $\pi/120$ | radians |
| Gradient at fiber boundary (minimum) | 35 | |
| Total fiber diameter (maximum) | 30 | μm |
| Myelin thickness (maximum) | 0.333 | |
| Structuring element radius | 1 | pixels |

correct axon labels. We developed manual correction tools for the deletion and addition of axons – based on prior knowledge of axon appearance, the user manually deleted axons by identifying mislabeled areas (Fig. 2(h)), and manually added axons by tracing their outline with similar accuracy to the algorithm (Fig. 2(i)). Using our manual correction methods and user interface, we corrected the inevitable errors in automatic segmentation before finalizing data for statistical analysis.

2.6. Output

Upon completion, our method had quantified the location and size of all myelinated axons and their corresponding myelin sheaths. We used this information to calculate the size of each myelinated nerve fiber as the diameter of a circle with equivalent area to the sum of the corresponding axon and myelin areas (Fig. 2(k)). Equivalent circle diameter was chosen as a measure of nerve fiber size because, in addition to being the most accurate method (Karnes et al., 1977), diameter is directly correlated with physiological properties of axons such as conduction velocity (Gasser and Grundfest, 1939; Hursh, 1939; Rushton, 1951). Since diameter is a commonly used size measure (Karnes et al., 1977; Ellis et al., 1980) this also allowed us to compare our measurements to those found in other studies. As well, we used the quantified information to calculate the total number of myelinated nerve fibers and extremes of myelinated nerve fiber size.

2.7. Performance

To illustrate the performance of these methods, we report results from the supervised semi-automated analysis of one average-sized fascicle, approximately 0.5 mm in diameter, from one rat sciatic nerve. We compare the results obtained using our semi-automated method with those obtained using a completely manual method in which we manually traced the outline of each

Table 2

Performance characteristics of supervised segmentation algorithm. The top section of the table shows the time of each step, and the bottom section shows the number of axons identified in relevant procedures. Processing times include the time needed to stitch and crop the image as well as perform automatic segmentation and manual correction, whereas segmentation times include only the time needed to perform automatic segmentation and manual correction. For comparison with our supervised method, we also present data obtained from manual analysis of the same fascicle, in which all nerve fibers were identified by tracing their outer edge by hand. Predicted whole-nerve segmentation time is based on a nerve having an area 4.5 times as large as the fascicle we analyzed. False positives are background areas mislabeled as axons by the automatic axon segmentation procedure, whereas false negatives are axons mislabeled as background.

| | Time (s) | Time (h:min:s) |
|--|----------|----------------|
| Time to automatically stitch | 12 | 00:00:12 |
| Time to manually crop | 206 | 00:03:26 |
| Time to automatically segment axons | 8 | 00:00:08 |
| Time to manually delete axons | 856 | 00:14:16 |
| Time to manually add axons | 2351 | 00:39:11 |
| Time to automatically segment myelin | 44 | 00:00:44 |
| Total processing time, one fascicle (supervised method) | 3477 | 00:57:57 |
| Total fiber segmentation time, one fascicle (supervised method) | 3259 | 00:54:19 |
| Total fiber segmentation time, one fascicle (manual method) | 25,445 | 07:04:05 |
| Predicted fiber segmentation time, whole nerve (supervised method) | 14,666 | 04:04:26 |
| Predicted fiber segmentation time, whole nerve (manual method) | 114,503 | 31:48:23 |
| # axons | | |
| Initially identified | 1963 | |
| Correctly identified | 1694 | |
| False positives | 269 | |
| False negatives | 316 | |
| Total in fascicle (supervised method) | 2010 | |
| Total in fascicle (manual method) | 2025 | |
| Predicted total in whole nerve (supervised method) | 9045 | |
| Predicted total in whole nerve (manual method) | 9113 | |

nerve fiber using a stylus and graphics tablet (Wacom Graphire 4, Wacom Co., Ltd., Saitama, Japan). The segmentation results are shown in Fig. 4, and performance metrics for each stage of analysis are given in Table 2. We implemented both semi-automated and manual methods in MATLAB (Mathworks, Natick MA) and performed all analyses on a PC with a 3.40 GHz Pentium D processor and 2GB of RAM. We manually deleted and added axons using a stylus and graphics tablet.

3. Results

To cover the entire fascicle, we collected 45 SEM images and stitched them together using our normalized cross-correlation algorithm (Fig. 4(a)). Of the 2010 axons ultimately identified in the fascicle (Fig. 4(b)), our automated axon segmentation algorithm correctly identified 84.3%, leaving 15.7% of axons unidentified – these false negatives were added using our manual correction tools. Of the 1963 potential axons initially identified by our automated axon segmentation algorithm, 13.4% were in fact background areas – these false positives were deleted using our manual correction tools. Our semi-automated method and the completely manual method identified 2010 axons and 2025 axons, respectively – a 0.5% difference.

After all axons had been identified, our automated myelin segmentation algorithm identified myelin surrounding 98.5% of the axons (Fig. 4(c)). The identified myelin was not always accurate, however. In cases where cracks appeared in the myelin, the algorithm ceased labeling at the crack. In cases where the boundary between myelin and background was indistinct, or where two

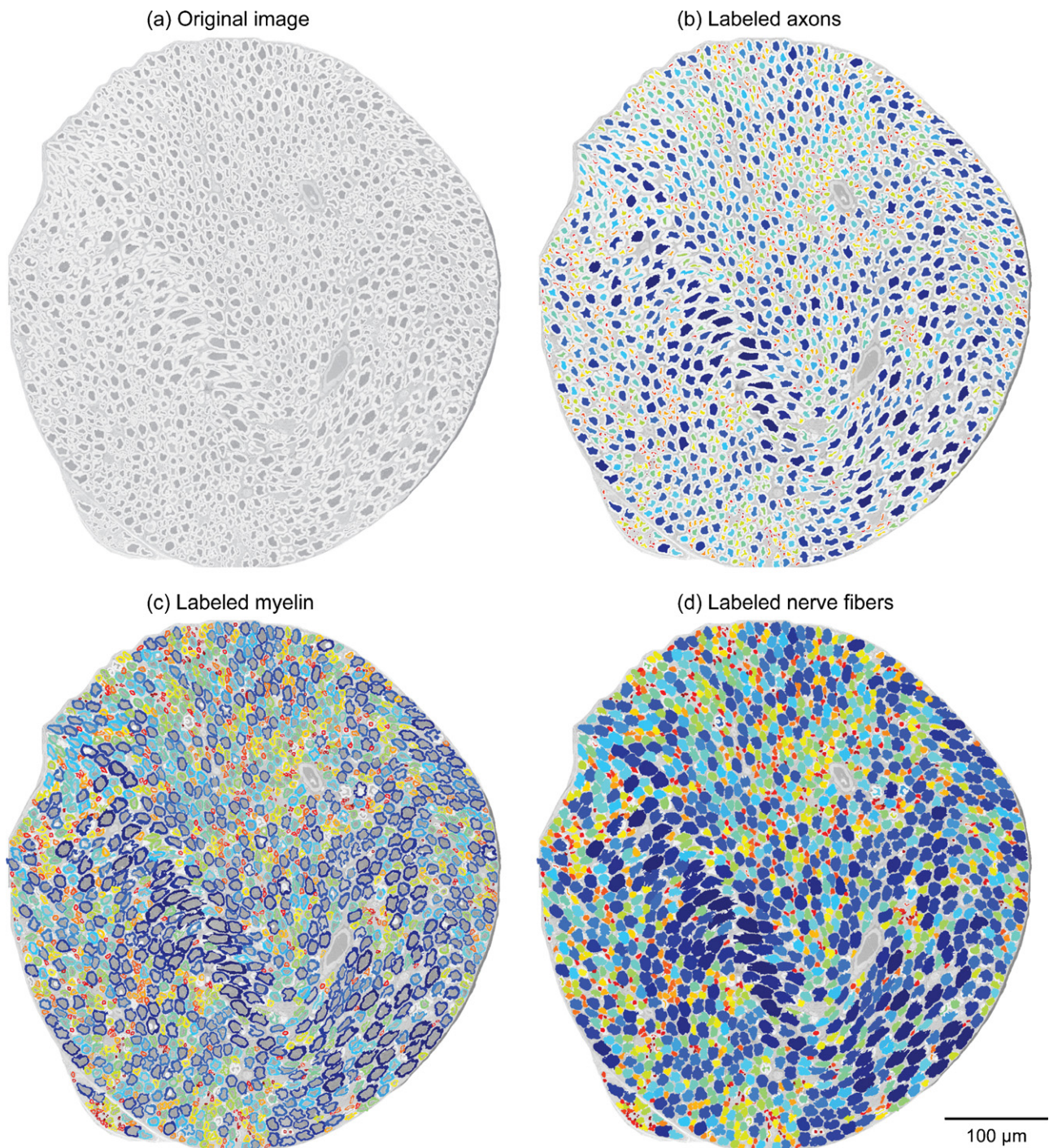


Fig. 4. Axon and myelin segmentation result for one rat fascicle. Following sub-image stitching (Fig. 1), we manually cropped the resulting image to remove extraneous surrounding information and give the original greyscale image (a) input into our algorithm. Our algorithm automatically identified the axons in the original image, after which we removed misidentified axons and added missing axons using our manual correction tools. Overlaying the final axon labels on the original image, as shown in (b), enabled visual evaluation of segmentation. Our algorithm then automatically identified the myelin surrounding each axon using a star algorithm. Overlaying the resulting myelin labels on the original image, as shown in (c), again allowed visual evaluation. Finally, we combined each labeled axon with its respective labeled myelin sheath to obtain labeled nerve fibers. We overlaid the resulting nerve fiber labels on the original image, as shown in (d).

myelin sheaths touched, the algorithm often continued labeling past the outer myelin border. Myelin surrounding 1.5% of axons was not identified. The majority of these axons had convoluted shapes in which the geometric center did not fall within the labeled axon area. Myelinated nerve fibers are shown as the merging of labeled axon and myelin areas in Fig. 4(d), with a histogram illustrating myelinated nerve fiber size distribution shown in Fig. 5.

As the number of axons in an image can vary, we found it useful to express the speed of our algorithm steps on a per-axon basis

in addition to reporting the overall speed of our method. Automatic identification of each potential axon by our algorithm took approximately 4 ms per axon, while manual deletion of one axon took approximately 3.2 s and manual addition took just over 7.4 s per axon. After axon identification, automatic myelin identification took approximately 22 ms per axon. The total time required to fully process the sample image was just under 1 h, including manual correction. Stitching the sub-images together comprised 0.3% of this time, manually cropping the fascicle comprised 5.9%,

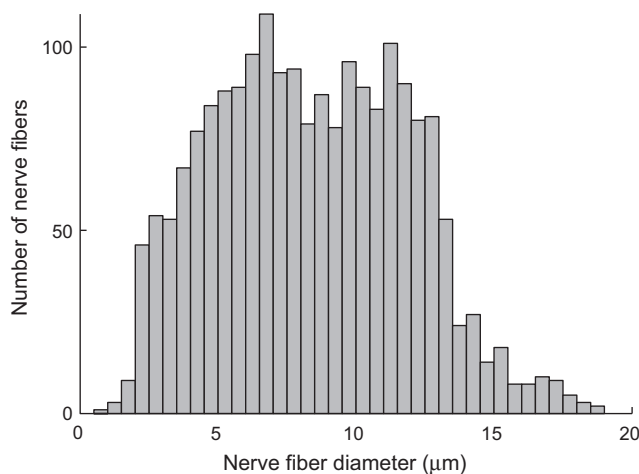


Fig. 5. Myelinated nerve fiber size distribution. Axon and myelin areas for the fascicle depicted in Fig. 3 were added to obtain nerve fiber area, which was then converted to equivalent nerve fiber diameter by considering a circle with equal area. The diameters of all 2010 nerve fibers in the fascicle are displayed as a histogram to allow evaluation of nerve fiber size distribution.

automatic segmentation comprised 0.2%, and manual deletion and addition comprised 24.6% and 67.6%, respectively. Identification of myelin comprised the remaining 1.3% of segmentation time. Our supervised segmentation method was approximately 7.8 times faster than completely manual segmentation of the entire fascicle, reducing the time required for the analysis of all nerve fibers in the fascicle from over 7 h to under 1 h. After automatic stitching of sub-images and cropping, we estimate that the time needed to segment the entire nerve (approximately 4.5 times the area of the fascicle) would be approximately 4.5 times as long, taking roughly 4 h using our supervised segmentation method as compared to almost 32 h using manual segmentation methods.

4. Discussion

Our supervised segmentation method is efficient. With a 7.8-fold increase in speed over traditional manual segmentation methods as well as the ability to identify both axon and myelin characteristics in every axon of a nerve, it markedly reduces the time and effort needed to analyze SEM images of nerve cross sections. The quality control tools help users quickly identify and correct any errors made by the algorithm, as well as visually evaluate the accuracy of the results. Due to our algorithm's ability to stitch together multiple SEM images into one larger image showing a whole nerve or fascicle cross-section, our method allows us to analyze an entire nerve or fascicle at one time. This eliminates the need to sample only a few regions of the nerve, reducing sampling error and producing more accurate data. While a time savings of over 27 h for small nerves (containing on the order of 10^4 axons) is quite substantial, we anticipate that the time savings for very large nerves (containing on the order of 10^5 axons) (More et al., 2010) will be even more impressive, potentially saving months of work.

One of the major advantages of our algorithm is its simplicity and ease of implementation. Methods of segmentation previously developed to analyze nerve images often use complex algorithms involving zonal graphs (Romero et al., 2000), clustering (Campadelli et al., 1999), and bit-plane analysis (Hunter et al., 2007). In contrast, our algorithm uses only basic morphological operators and reconstructions, making it highly customizable, computationally efficient, and easy to understand and execute in a wide range of software programs. Additionally, the input parameters for the automated portions of our algorithm are based on physiological properties, making them intuitive and our method easy to learn.

These factors allow almost anyone to employ our segmentation method without the investment of a large amount of time and money. Our method provides a straightforward workflow that most clinicians and researchers can use. While our method has a slightly longer analysis time than some others (Romero et al., 2000; Hunter et al., 2007), its use of SEM imaging and simplicity of implementation make it a worthy addition to existing methods of nerve segmentation.

Applying our method to a sample rat sciatic nerve produces results similar to those of other researchers. Our results demonstrate the classic bimodal distribution of myelinated fibers in peripheral nerves (Bronson et al., 1978), and the shape of our histogram (Fig. 5) is similar to that obtained in previous studies of the rat sciatic nerve (Schmalbruch, 1986). Although nerve fibers found by our algorithm are larger on average than those in other studies (Schmalbruch, 1986; Hunter et al., 2007), we attribute this to the nature of the sample used rather than to any error in our algorithm. The sample included several regions of large elongated axons, and because our method identifies and measures every axon in the nerve rather than several representative areas these outliers will tend to skew our distribution towards larger axon sizes. In fact, we view this as a strength of our method – rather than extrapolating from a limited sample set, as in most other studies, all axons, including those with noncircular or irregular shapes are identified. Our results predict a total of slightly more than 9100 axons in the rat sciatic nerve, which is within the range of axon numbers found in other studies (Schmalbruch, 1986).

Although our method is an improvement over existing methods, it is not without limitations. Our axon segmentation algorithm is very efficient and automatically identifies the majority of axons, but there are still quite a few false positives (background areas identified as axons) and false negatives (missed axons). This underscores the need for supervision of segmentation – the inherent variability in biological samples means that manual input, rather than a completely automated method, is required to get accurate results. Accurate tuning of parameters helps to reduce the total number of false positives and false negatives. It is important to note that the time required to re-analyze the image after each iterative adjustment is only 8 s, making parameter tuning a rapid process.

Our myelin segmentation algorithm is based on three assumptions: firstly that the thickness of myelin around each axon varies only within a small range, secondly that the myelin surrounding different axons does not touch each other, and thirdly that there are no cracks, clefts, or excessive noise in the myelin. However, these assumptions are not always true. In the first case, if the myelin thickness is very irregular the algorithm may underestimate the thickness of wider myelin areas. In the second case, if the myelin of different axons touches each other the algorithm may not detect the boundary between the two myelin areas and may fail to stop scanning, resulting in an overestimation of myelin area. In the third case, the algorithm may detect the myelin boundary too soon, resulting in an underestimation of myelin area. Setting a maximum myelin thickness helps solve the second problem, but makes the first problem worse. Similarly, raising the gradient threshold for detecting the edge of the myelin helps solve the third problem but makes the second problem worse. More sophisticated methods such as active contours (Fok et al., 1996) may help solve these problems and improve accuracy by growing a continuous smooth line outward from the axon perimeter and using criteria based on smoothness and thickness to detect when the outer myelin edge is reached.

Like most automated image segmentation methods, the performance of our method depends heavily on image quality. Due to variability in tissue characteristics, small but unavoidable differences in nerve processing between animals, and sample height differences in the SEM itself, images acquired from each nerve are slightly different. Differences in contrast between axons, myelin,

and background are the most common, and differences in noise level are also present. This variation requires manual adjustment of parameters for each image to achieve the highest accuracy, however each adjustment can be made very quickly due to our algorithm's speed. A potentially productive future area of research is the development of an automated method to optimize parameter values using training data, for example a small manually segmented section of the nerve image.

In addition to our presented data on total nerve fiber size, other characteristics such as nerve fiber shape, spatial distribution of nerve fiber sizes throughout the fascicle and nerve, and the axon/myelin ratio are readily available for output from our method. These techniques therefore have the potential to be useful for a wide range of applications including studies of nerve structure, function, and response to injury. The high efficiency of our method enables the fast, accurate, and comprehensive study of nerves from humans and other large animals which are currently not feasible. Because whole-nerve analysis measures nerve characteristics directly, rather than approximating them from small sample areas, a more accurate description of the nerve fiber population within the nerve is possible and may allow the identification of subtle differences between specimens. This is especially useful for clinical and comparative studies, and may greatly enhance the understanding of nervous system organization and function.

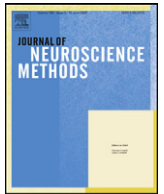
Acknowledgements

The authors thank Winnie Enns for assistance with nerve acquisition and processing. This work was funded by a NSERC graduate scholarship to HLM; a MSFHR Career Investigator Award, CIHR New Investigator Award and NSERC Discovery Grant to JMD; and a MSFHR Career Investigator Award and NSERC Discovery Grant to MFB.

References

- Arbuthnott ER, Ballard KJ, Boyd IA, Kalu KU. Quantitative study of the non-circularity of myelinated peripheral nerve fibres in the cat. *J Physiol* 1980a;308:99–123.
- Arbuthnott ER, Boyd IA, Kalu KU. Ultrastructural dimensions of myelinated peripheral nerve fibres in the cat and their relation to conduction velocity. *J Physiol* 1980b;308:125–57.
- Auer RN. Automated nerve fibre size and myelin sheath measurement using microcomputer-based digital image analysis: theory, method and results. *J Neurosci Methods* 1994;51:229–38.
- Boyd IA, Kalu KU. Scaling factor relating conduction velocity and diameter for myelinated afferent nerve fibres in the cat hind limb. *J Physiol* 1979;289:277–97.
- Bronson RT, Bishop Y, Hedley-Whyte ET. A contribution to the electron microscopic morphometric analysis of peripheral nerve. *J Comp Neurol* 1978;178:177–86.
- Bronson RT, Hedley-Whyte ET. Morphometric analysis of the effects of exenteration and enucleation on the development of third and sixth cranial nerves in the rat. *J Comp Neurol* 1977;176:315–29.
- Campadelli P, Gangai C, Pasquale F. Automated morphometric analysis in peripheral neuropathies. *Comput Biol Med* 1999;29:147–56.
- Demirer S, Kepenekci I, Evrigen O, Birsan O, Tuzuner A, Karahuseynoglu S, et al. The effect of polypropylene mesh on ilioinguinal nerve in open mesh repair of groin hernia. *J Surg Res* 2006;131:175–81.
- Dunn HF, O'Leary DP, Kumley WE. Quantitative analysis of micrographs by computer graphics. *J Microsc* 1975;105:205–13.
- Edds Jr MV. Hypertrophy of nerve fibers to functionally overloaded muscles. *J Comp Neurol* 1950;93:259–75.
- Ellis TJ, Rosen D, Cavanagh JB. Automated measurement of peripheral nerve fibres in transverse section. *J Biomed Eng* 1980;2:272–80.
- Ewart DP, Kuzon Jr WM, Fish JS, McKee NH. Nerve fibre morphometry: a comparison of techniques. *J Neurosci Methods* 1989;29:143–50.
- Fok YL, Chan JK, Chin RT. Automated analysis of nerve-cell images using active contour models. *IEEE Trans Med Imaging* 1996;15:353–68.
- Fraher JP. On methods of measuring nerve fibres. *J Anat* 1980;130:139–51.
- Fried K, Hildebrand C. Axon number and size distribution in the developing feline inferior alveolar nerve. *J Neurol Sci* 1982;53:169–80.
- Fried K, Hildebrand C, Erdelyi G. Myelin sheath thickness and internodal length of nerve fibres in the developing feline inferior alveolar nerve. *J Neurol Sci* 1982;54:47–57.
- Friede RL. Computer editing of morphometric data on nerve fibers. An improved computer program. *Acta Neuropathol* 1986;72:74–81.
- Friede RL, Beuche W. A new approach toward analyzing peripheral nerve fiber populations. I. Variance in sheath thickness corresponds to different geometric proportions of the internodes. *J Neuropathol Exp Neurol* 1985;44:60–72.
- Frykman GK, Rutherford HG, Neilsen IR. Automated nerve fiber counting using an array processor in a multi-minicomputer system. *J Med Syst* 1979;3:81–94.
- Gasser HS, Grundfest H. Axon diameters in relation to the spike dimensions and the conduction velocity in mammalian A fibers. *Am J Physiol* 1939;127:393–414.
- Haralick RM, Shapiro LG. Computer and Robot Vision. Addison-Wesley; 1992.
- Hildebrand C, Hahn R. Relation between myelin sheath thickness and axon size in spinal cord white matter of some vertebrate species. *J Neurol Sci* 1978;38:421–34.
- Hoffmeister B, Janig W, Lisney SJ. A proposed relationship between circumference and conduction velocity of unmyelinated axons from normal and regenerated cat hindlimb cutaneous nerves. *Neuroscience* 1991;42:603–11.
- Hunter DA, Moradzadeh A, Whitlock EL, Brenner MJ, Myckatyn TM, Wei CH, et al. Binary imaging analysis for comprehensive quantitative histomorphometry of peripheral nerve. *J Neurosci Methods* 2007;166:116–24.
- Hursh JB. Conduction velocity and diameter of nerve fibers. *Am J Physiol* 1939;127:127.
- Jeong WK, Beyer J, Hadwiger M, Vazquez A, Pfister H, Whitaker RT. Scalable and interactive segmentation and visualization of neural processes in EM datasets. *IEEE Trans Vis Comput Graph* 2009;15:1505–14.
- Jurjus E, Paiva ARC, Watanabe S, Anderson JR, Jones BW, Whitaker RT, et al. Detection of neuron membranes in electron microscopy images using a serial neural network architecture. *Med Image Anal* 2010;14:770–83.
- Karnes J, Robb R, O'Brien PC, Lambert EH, Dyck PJ. Computerized image recognition for morphometry of nerve attribute of shape of sampled transverse sections of myelinated fibers which best estimates their average diameter. *J Neurol Sci* 1977;34:43–51.
- Knox CA, Kokmen E, Dyck PJ. Morphometric alteration of rat myelinated fibers with aging. *J Neuropathol Exp Neurol* 1989;48:119–39.
- Larsen JO. Stereology of nerve cross sections. *J Neurosci Methods* 1998;85:107–18.
- Lewis JP. Fast normalized cross-correlation. *Vis Interface* 1995.
- McCreery DB, Yuen TGH, Agnew WF, Bullara LA. A quantitative computer-assisted morphometric analysis of stimulation-induced injury to myelinated fibers in a peripheral nerve. *J Neurosci Methods* 1997;73:159–68.
- Mezin P, Tenaud C, Bosson JL, Stoebner P. Morphometric analysis of the peripheral nerve: advantages of the semi-automated interactive method. *J Neurosci Methods* 1994;51:163–9.
- More HL, Hutchinson JR, Collins DF, Weber DJ, Aung SK, Donelan JM. Scaling of sensorimotor control in terrestrial mammals. *Proc Biol Sci* 2010.
- Romero E, Cuisenaire O, Denef JF, Delbeke J, Macq B, Veraart C. Automatic morphometry of nerve histological sections. *J Neurosci Methods* 2000;97:111–22.
- Rushton WA. A theory of the effects of fibre size in medullated nerve. *J Physiol* 1951;115:101–22.
- Saxod R, Torch S, Vila A, Laurent A, Stoebner P. The density of myelinated fibres is related to the fascicle diameter in human superficial peroneal nerve. Statistical study of 41 normal samples. *J Neurol Sci* 1985;71:49–64.
- Schmalbruch H. Fiber composition of the rat sciatic nerve. *Anat Rec* 1986;215:71–81.
- Smith KJ, Blakemore WF, Murray JA, Patterson RC. Internodal myelin volume and axon surface area. A relationship determining myelin thickness? *J Neurol Sci* 1982;55:231–46.
- Sullivan KA, Brown MS, Harmon L, Greene DA. Digital electron microscopic examination of human sural nerve biopsies. *J Peripher Nerv Syst* 2003;8:260–70.
- Tasdzien T, Koshevoy P, Grimm BC, Anderson JR, Jones BW, Watt CB, et al. Automatic mosaicking and volume assembly for high-throughput serial-section transmission electron microscopy. *J Neurosci Methods* 2010;193:132–44.
- Torch S, Stoebner P, Usson Y, D'Aubigny GD, Saxod R. There is no simple adequate sampling scheme for estimating the myelinated fibre size distribution in human peripheral nerve: a statistical ultrastructural study. *J Neurosci Methods* 1989a;27:149–64.
- Torch S, Usson Y, Saxod R. Automated morphometric study of human peripheral nerves by image analysis. *Pathol Res Pract* 1989b;185:567–71.
- Urso-Baiarda F, Grobbelaar AO. Practical nerve morphometry. *J Neurosci Methods* 2006;156:333–41.
- Usson Y, Torch S, Saxod R. Morphometry of human nerve biopsies by means of automated cytometry: assessment with reference to ultrastructural analysis. *Anal Cell Pathol* 1991;3:91–102.
- Vincent L. Morphological greyscale reconstruction in image analysis: applications and efficient algorithms. *IEEE Trans Image Process* 1993;2:176–201.
- Vogt RC. Robust extraction of axon fibers from large-scale electron micrograph mosaics. In: Maragos P, editor. *Mathematical Morphology and its Applications to Image and Signal Processing*. Norwell, Massachusetts: Kluwer Academic Publishers; 1996. p. 433–41.
- Vogt RC, Trenkle JM. Mosaic construction, processing, and review of very large electronic micrograph composites. USA: Frim International, Inc; 1998. p. 12.
- Wattig B, Schalow G, Heydenreich F, Warzok R, Cervos-Navarro J. Enhancement of nerve fibre regeneration by nucleotides after peripheral nerve crush damage. Electrophysiologic and morphometric investigations. *Arzneimittelforschung* 1992;42:1075–8.
- Webster HD. The geometry of peripheral myelin sheaths during their formation and growth in rat sciatic nerves. *J Cell Biol* 1971;48:348–67.

- Weyn B, van Remoortere M, Nuydens R, Meert T, van de Wouwer G. A multiparametric assay for quantitative nerve regeneration evaluation. *J Microsc* 2005;219:95–101.
- Yao W, Tian J, Zhao B, Chen N, Qian G. Star algorithm: detecting the ultrasonic endocardial boundary automatically. *Ultrasound Med Biol* 2004;30:943–51.
- Zhao X, Pan Z, Wu J, Zhou G, Zeng Y. Automatic identification and morphometry of optic nerve fibers in electron microscopy images. *Comput Med Imaging Graph* 2010;34:179–84.
- Zimmerman IR, Karnes JL, O'Brien PC, Dyck PJ. Imaging system for nerve and fiber tract morphometry: components, approaches, performance, and results. *J Neuropathol Exp Neurol* 1980;39:409–19.



Erratum

Erratum to “A semi-automated method for identifying and measuring myelinated nerve fibers in scanning electron microscope images” [J. Neurosci. Methods 201 (2011) 149–158]

Heather L. More^{a,*}, Jingyun Chen^{b,1}, Eli Gibson^b, J. Maxwell Donelan^a, Mirza Faisal Beg^b

^a Department of Biomedical Physiology & Kinesiology, Simon Fraser University, 8888 University Drive, Burnaby, BC V5A 1S6, Canada

^b School of Engineering Science, Simon Fraser University, 8888 University Drive, Burnaby, BC V5A 1S6, Canada

The Publisher regrets that in the above mentioned paper, the equation in Section 2.2 was incorrectly printed. The corrected equation is reproduced below.

$$\text{Normalized cross-correlation } (u, v) = \frac{\sum_{x,y} (I_0(x-u, y-v) - \bar{I}_0(u, v))(I_1(x, y) - \bar{I}_1(u, v))}{\sqrt{\sum_{x,y} (I_0(x-u, y-v) - \bar{I}_0(u, v))^2 \sum_{x,y} (I_1(x, y) - \bar{I}_1(u, v))^2}}$$

DOI of original article: [10.1016/j.jneumeth.2011.07.026](https://doi.org/10.1016/j.jneumeth.2011.07.026).

* Corresponding author. Tel.: +1 778 782 4986; fax: +1 778 782 3040.

E-mail address: hmore@sfu.ca (H.L. More).

¹ These authors contributed equally to this work.